

Article

A Nonlinear Impact-Driven Triboelectric Vibration Energy Harvester for Frequency Up-Conversion

Hadeel Abumarar and Alwathiqbellah Ibrahim * 

Department of Mechanical Engineering, University of Texas at Tyler, 3900 University Blvd., Tyler, TX 75799, USA
* Correspondence: aibrahim@uttyler.edu

Abstract: Energy harvesting effectively powers micro-sensors and wireless applications. However, higher frequency oscillations do not overlap with ambient vibrations, and low power can be harvested. This paper utilizes vibro-impact triboelectric energy harvesting for frequency up-conversion. Two magnetically coupled cantilever beams with low and high natural frequencies are used. The two beams have identical tip magnets at the same polarity. A triboelectric energy harvester is integrated with the high-frequency beam to generate an electrical signal via contact-separation impact motion between the triboelectric layers. An electrical signal is generated at the low-frequency beam range achieving frequency up-converter. The two degrees of freedom (2DOF) lumped-parameter model system is used to investigate the system's dynamic behavior and the corresponding voltage signal. The static analysis of the system revealed a threshold distance of 15 mm that divides the system into monostable and bistable regimes. In the monostable and bistable regimes, softening and hardening behaviors were observed at low frequencies. Additionally, the threshold voltage generated was increased by 1117% in comparison with the monostable regime. The simulation findings were experimentally validated. The study demonstrates the potential of using triboelectric energy harvesting in frequency up-converting applications.

Keywords: frequency up; triboelectric; energy harvesting; up-conversion; transition; magnet



Citation: Abumarar, H.; Ibrahim, A. A Nonlinear Impact-Driven Triboelectric Vibration Energy Harvester for Frequency Up-Conversion. *Micromachines* **2023**, *14*, 1082. <https://doi.org/10.3390/mi14051082>

Academic Editor: Wei Li

Received: 30 March 2023

Revised: 26 April 2023

Accepted: 18 May 2023

Published: 20 May 2023



Copyright: © 2023 by the authors. Licensee MDPI, Basel, Switzerland. This article is an open access article distributed under the terms and conditions of the Creative Commons Attribution (CC BY) license (<https://creativecommons.org/licenses/by/4.0/>).

1. Introduction

Modern science and technology have advanced quickly, leading to a substantial rise in ultra-low-powered electronics across various industries. This increases public knowledge of ambient energies and creates a sizable market for them as potential sources to replace chemical batteries in these devices [1]. Using renewable energy sources, such as solar energy [2], radio frequency (RF) [3], thermal energy [4], and mechanical vibration energy [5], the principle of energy harvesting provides a way to power small devices. Mechanical vibrations occur naturally at low frequencies, as do ambient energies in our surroundings such as wind [6,7], ocean waves [8], human and vehicle movement [9,10], and working equipment, which has frequencies between 1 and 200 Hz [11].

There are a variety of mechanisms that have been utilized to harvest vibrational energy for electricity generation, including electrostatic transduction mechanisms [12,13], piezoelectric [14], electromagnetic [15,16], and triboelectric generators [17–19]. Triboelectric generators have some advantages for vibration energy harvesting since Wang's team created the first triboelectric nanogenerator in 2012 [20]. These advantages include high output voltage, low cost, the flexibility of fabrication, and effective energy scavenging from low vibration frequencies [21,22]. Furthermore, triboelectric energy harvesters have shown great potential for capturing energy from a range of sources, such as human movement [23,24], mechanical vibration [25], smart home applications [26], wearable technology [27–30], implantable medical devices [31–34], and wireless sensor networks (WSN) [35–37]. Furthermore, triboelectric energy harvesting effectively converts small amounts of kinetic energy into electricity, typically in the microwatt range, under the influence of impact.

Overall, triboelectric generators operate in four different ways, namely the in-plane sliding mode [38,39], the single electrode mode [40,41], the free-standing triboelectric layer mode [42,43], and the vertical contact separation mode [44,45] that have been used in this study.

Even though the harvested energy from the ambient vibrations appears to be high with high-efficiency conversion devices, some devices' resonant frequencies do not match the frequency of the ambient vibrations or the bandwidth is limited to a specific range. As a result, if the device's frequency deviates slightly from the harvester's resonant frequency, the harvested power will drop significantly [46]. Additionally, according to its general mathematical formula, the energy harvester's highest power is proportionate to the cube of its vibration frequency and decreases significantly at low frequencies [47]. Moreover, most environmental vibration energies in real-world situations are dispersed over narrow frequency ranges [48–50]. Therefore, researchers have spent considerable time and effort finding solutions to the above-mentioned issues [51]. Therefore, a frequency up-converter to transform low excitations into high-frequency oscillations was suitable for energy harvesting applications. However, frequency-up conversions were traditionally achieved either using contact mechanisms or non-contact impulse accelerations [52,53]. This led to the development of mechanical impact frequency up-converters with direct contact [54,55]. Frequency-up converters were used for energy harvesting applications utilizing different approaches such as snap-through buckling [56] and bistable oscillations [57]. Recently, Yin et al. [58] presented a shoe that harvests energy from human motion using a mounted piezoelectric energy harvester with frequency-up conversion. Furthermore, Atmeh et al. [14,59] investigated theoretically and experimentally a piezoelectric frequency up-converter mechanism for harvesting energy at ambient range utilizing high-frequency oscillations.

This paper proposed a frequency up-converter to harvest low-frequency vibrations utilizing a triboelectric generator and magnetic coupling. The frequency-up converter mainly consists of two cantilever beams coupled with two identical magnets attached to the tip of the beams. The tip magnets are attached facing each other at the same polarity to provide a nonlinear repulsive magnetic force responsible for converting low-frequency vibrations into high-frequency oscillations. A two-degree of freedom (2DOF) lumped parameter model has been used to investigate the beam's dynamic behavior and the produced voltage signal. The rest of this article describes the device's setup and demonstrates how the frequency-up-converter energy harvester operates. In addition, each beam's static response and the frequency variations caused by the magnet separation distance and the generation of voltage and power at different values of the magnet separation distance are investigated. Experiments are also carried out to validate the simulation results derived from the theoretical model. In the end, the optimum operation region is determined.

2. Device Configuration and Principle of Operation

The 2DOF triboelectric energy harvester consists of two cantilever beams, as shown in Figure 1a. The left side beam is made of polymer with a low natural frequency and is called, for simplicity, a low-frequency beam (LFB), while the right side beam is made of aluminum with a higher natural frequency and is called a high-frequency beam (HFB). For each beam, a magnet is attached to the tip, where the magnets face each other at the same polarity to provide a nonlinear mechanical repulsive magnetic force. The magnetic force transfers the energy from the high-frequency to low-frequency range achieving the concept of frequency up-conversion. L_1 and L_2 are the lengths of the (LFB) and (HFB), respectively. Both tip magnets attached to the beams are separated by the distance d . The whole setup is attached to a holder and installed in an electrodynamic shaker to provide an excitation source to the system. The triboelectric generator mainly consists of three layers: a lower fixed electrode made of aluminum with attached Polydimethylsiloxane (PDMS) insulator layer and an upper aluminum electrode attached to the bottom surface of the HFB's tip magnet. The upper electrode and the insulator layer are separated by an initial gap g_i , while

the two electrodes are separated by a distance d_0 . Once the system starts vibrating under harmonic excitation $a(t)$, the upper electrode periodically impacts the insulator, generating an electrical signal based on contact electrification and electrostatic induction [60].

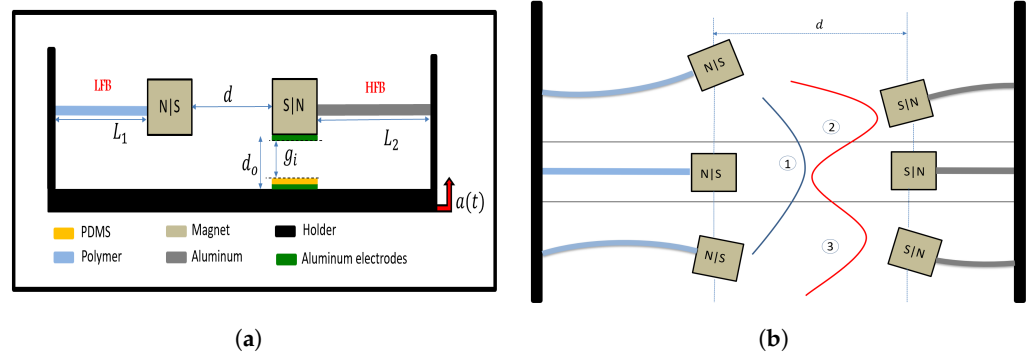


Figure 1. (a) 2D schematic of the energy harvester system; (b) Device operation under repulsive magnetic force.

Figure 1b depicts how the distance between magnets impacts the beam’s response and potential energy function. The magnetic force varies based on the separation distance and generates an additional equilibrium point, resulting in a bistable system. The potential energy function can either be a single well or a double well, depending on the distance between magnets. For greater distances between magnets, the beam exhibits monostable behavior, oscillating about a single stable point, i.e., point 1. At shorter distances, the system has two potential wells, and the beam oscillates between two stable equilibrium points, namely points 2 and 3, indicating bistable behavior. The critical separation distance that divides the monostable and bi-stable systems is called the threshold distance, or d_{th} .

3. Theoretical Model

Under mechanical excitation, the system will vibrate and generate electrical signal voltage due to the contact and separation between the harvester layers, Figure 2. Moreover, a repulsive force with the same magnitude will be induced between the two identical tip magnets, transferring the energy between both beams and given by Equation (1). Therefore, the total repulsive magnetic force can be analyzed into two components through the angle ϕ as shown in Figure 2. The first component is (F_{magx}) in the horizontal direction, which is assumed to have a minor effect on the transverse vibrations and balancing the longitudinal stiffness of the beam, and it will be neglected for simplicity. In contrast, the second component is (F_{magy}) in the vertical direction, which is assumed to be the only component responsible for the transverse deflections of the beams. Then, the transverse magnetic force will be as given in Equation (2). Where X is the distance between the centers of the two magnets ($X = \sqrt{d^2 + Y^2}$), F_R is the magnitude of the moments for the magnetic force and can be calculated from ($F_R = \frac{3\mu q_1 q_2}{2\pi}$), where q_1 and q_2 are the moments of the magnetic dipoles for the tip magnets, μ is the permeability of the free space with a value of ($4\pi \times 10^{-7} \text{ mkg/s}^2\text{A}^2$). Moreover, d is the horizontal separation distance between the tip magnets, and Y is the total deflection of the beams and is given by $Y = z_1(t) + z_2(t)$, where z_1 and z_2 are the deflection of the LFB and HFB, respectively.

$$F_{mag} = \frac{F_R}{X^4} \sin \phi \tag{1}$$

$$F_{magy} = \frac{F_R Y}{(d^2 + Y^2)^{5/2}} \tag{2}$$

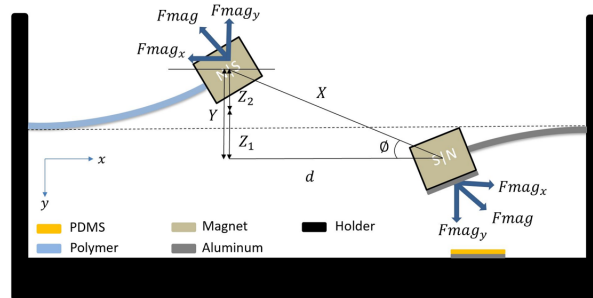


Figure 2. Magnetic interaction between the LFB and HFB.

A lumped parameter model of a two-degree of freedom (2DOF) system, shown in Figure 3, will be used to analyze the dynamic behavior and the generated electrical signal. Under vibration, the system will behave under two scenarios of motion, the first scenario is before impact, as shown in Figure 3a, and this occurs when the deflection of the HFB is not enough to reach the insulator layer (the tip magnet displacement less than the gap g_i). The second scenario is in the state of impact as shown in Figure 3b. The impact occurs when the upper electrode contacts the PDMS layer (the tip magnet displacement exceeds the gap g_i). This impact will increase the stiffness and the damping of the HFB, and this increment is expressed in k_i and c_i to be added to the system to represent the impact stiffness and impact damping, respectively. Accordingly, the governing equation of the system will be as follows [17]:

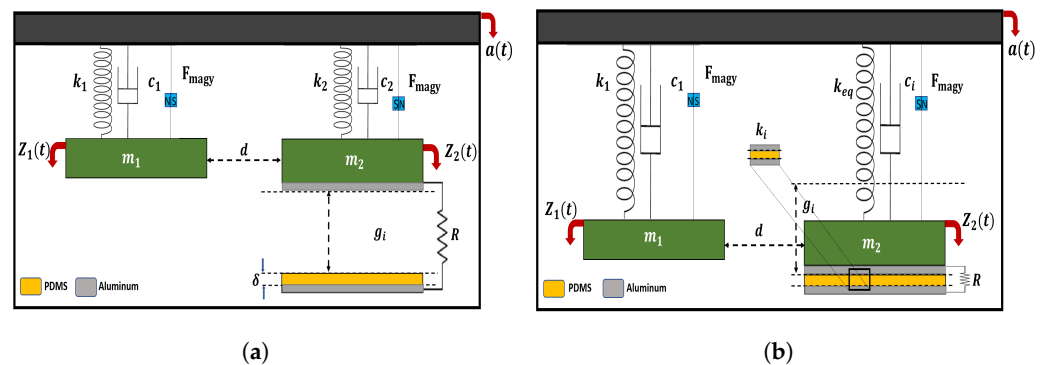


Figure 3. 2DOF spring-mass-damper systems for the LFB and HFB: (a) before impact; (b) after impact.

$$\begin{cases} m_1 \ddot{z}_1(t) + c_1 \dot{z}_1(t) + k_1 z_1(t) - F_{magy} = m_1 a(t) \\ m_2 \ddot{z}_2(t) + c_2 \dot{z}_2(t) + k_2 z_2(t) + F_{magy} + F_e = m_2 a(t) & z_2(t) < g_i \\ m_2 \ddot{z}_2(t) + c_i \dot{z}_2(t) + k_2 z_2(t) + k_i(z_2(t) - g_i) + F_{magy} = m_2 a(t) & z_2(t) \geq g_i \end{cases} \quad (3)$$

$$\dot{q} = -\frac{q(t)}{\epsilon_0 R S} \left(\frac{T}{\epsilon_r} + d_0 - z_2(t) \right) + \frac{\sigma}{\epsilon_0 R S} (d_0 - z_2(t))$$

where $a(t)$ is the harmonic base excitation ($a(t) = A \cos(\Omega t)$) with A is the amplitude, and Ω is the excitation frequency. The LFB's equivalent mass and damping coefficient are given by m_1 and c_1 , respectively, while m_2 and c_2 are the equivalent mass and the damping coefficient, respectively, of the HFB. k_1 is the equivalent stiffness of the LFB with tip magnet mass and is calculated by ($k_1 = \frac{3E_1 I_1}{L_1^3}$) [59], while k_2 is the equivalent stiffness of the HFB with tip magnet mass and is calculated by ($k_2 = \frac{3E_2 I_2}{L_2^3}$) [59]. In addition, the electrostatic force between the electrodes of the triboelectric energy harvester as they act as a parallel plate capacitor and is given by ($F_e = \frac{q^2(t)}{2\epsilon_0 \epsilon_r S}$). Moreover, k_i and c_i are the stiffness and capacitance during the impact scenario of the HFB. The electrical charges ($q(t)$) are transferred between the two electrodes. Moreover, ϵ_0 and ϵ_r are the permeability of the free space and the insulator, respectively. Finally, S , σ , and T are the surface area of contact, the

surface charge density, and the thickness of the insulator, respectively. Accordingly, the following formula can be used to calculate both beam's linear natural frequencies:

$$f_i = \frac{1}{2\pi} \sqrt{\frac{k_i}{m_i}}, \quad i = 1, 2. \quad (4)$$

where k_i and m_i are the effective mass and stiffness of the beams, respectively. The effective mass of the cantilever beam ($m_{heff} = 0.375m_b$) [59], where m_b is the beam mass.

It is worth mentioning that under the effect of the tip mass and base excitations enough to achieve the impact scenario as shown in the operation of the harvester, Figure 3, the upper electrode will come into contact with the lower PDMS electrode, generating electricity based on contact electrification and electrostatic induction. Under this condition, the beam will be bent, and the upper electrode will contact the lower insulator at a nonzero contact angle (not flat-to-flat surface contact). Therefore, a negative effect on the amount of energy harvested is expected. However, this issue is only shown at low excitations that result in a slight contact, while at high excitations, the inertia effect will be maximized, the two layers will contact each other perfectly, and the angle of contact will be almost zero. Moreover, we selected the material of the high-frequency beam (HFB) to be stiffer than the low-frequency beam (LFB) to achieve both high and low frequencies. However, we designed the HFB to be long to give extra flexibility in the structure and achieve the maximum possible contact between the triboelectric layers by minimizing the contact angle. Therefore, for simplicity, this effect has been neglected.

4. Experimental Setup

To experimentally validate the numerical results from the theoretical model, we use the setup shown in Figure 4 to test the system under different excitation levels and frequencies. The main components of the setup are the VR9500 control unit, amplifier, electrodynamics shaker, and triboelectric energy harvesting system. First, the controller unit regulates the base excitation applied by the shaker to control its amplitude and frequency. Then, the control unit sends signals to the amplifier for amplification before transferring them to the shaker that transfers the base excitation to the triboelectric energy harvester. As the triboelectric energy harvester system is subjected to base excitations from the shaker, it oscillates, and an impact between triboelectric layers starts generating electricity. Moreover, the accelerometers mounted on the tip magnets of each beam are connected to the VR9500 control unit and measure the deflection of the LFB and HFB beams to extract the frequency response and voltage curves. Finally, using the parameter listed in Table 1, the static and dynamic behaviors of the system can be extracted numerically.

Table 1. Physical and geometrical parameters to be used in the modified model.

Parameters	Symbol	Value
LFB (length × width × thickness)	$L_1 \times b_1 \times h_1$	$(38 \times 10 \times 1)$ mm
LFB Young's modulus	E_1	2.344 Gpa
LFB Density	ρ_1	1220 kg/m ³
LFB Damping coefficient	c_1	0.1 N.s/m
HFB (length × width × thickness)	$L_2 \times b_2 \times h_2$	$(75 \times 10 \times 1)$ mm
HFB Young's modulus	E_2	69.0 Gpa
HFB Density	ρ_2	2700 kg/m ³

Table 1. Cont.

Parameters	Symbol	Value
HFB Damping coefficient	c_2	0.1 N.s/m
Impact damping coefficient	c_i	$3.4 c_2$ N.s/m
Impact stiffness coefficient	k_i	$3.4 k_2$ N/m
Gap between Upper electrode and PDMS layer	g_i	0.001 m
Dimensions of PDMS layer (length \times width \times thickness)	$L_p \times b_p \times h_p$	$(10 \times 10 \times 0.04)$ mm
PDMS dielectric constant	ϵ_r	0.0001
Magnets side length	L_m	8 mm
Magnetic moment	$q_1 = q_2$	$0.5 \text{ A}^2/\text{m}$
Resistance	R	10 M Ω
Permeability of free space	ϵ_0	8.854×10^{-12}

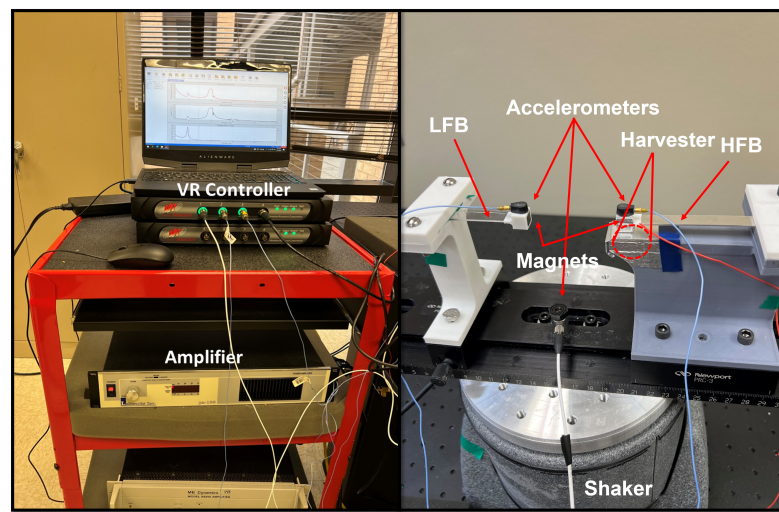


Figure 4. Experimental setup used to test the triboelectric energy harvester frequency-up converter.

5. Results and Discussion

5.1. Static Analysis

Since the repulsive magnetic force affects both beams statically, it is essential to investigate the static response of both beams as a function of the magnet spacing distance. Therefore, the static analysis of both beams can be formulated by setting all-time derivatives in Equation (3) to zero and replacing the base excitation with the gravitational acceleration (g) to include the weight effect. The weight affects only the static response, while it does not affect the dynamic response other than introducing a new equilibrium position [61]. Therefore, the static equations are given as follows:

$$k_1 z_{1s} - F_{magys} - m_1 g = 0 \quad (5)$$

$$k_2 z_{2s} + F_{magys} - m_2 g = 0 \quad (6)$$

where z_{1s} and z_{2s} are the static deflections of the LFB and HFB, respectively. F_{magys} is the static magnetic force in the transverse direction and is given by:

$$F_{magys} = \frac{F_R(z_{1s} + z_{2s})}{((z_{1s} + z_{2s})^2 + d^2)^{5/2}} \quad (7)$$

At large distances between the two magnets, the magnetic force is negligible. Therefore, each beam only undergoes a static equilibrium deflection due to the tip weight effect, which is also still considered very small. However, by lowering the separation distance between the two magnets to the threshold distance, both beams start to deflect from their previous

equilibrium points to settle to new equilibrium points due to the effect of the magnetic force induced by lowering magnet spacing. By varying the distance between the two magnets, the corresponding static equilibrium points can be extracted numerically by solving for the roots of Equation (7) and experimentally by measuring the vertical deflections of both beams from the initial horizontal axis with a ruler. The experimental and theoretical variation of the static deflection for the LFB and HFB tip magnet centers with varying the distance between them are shown in Figure 5 with a good agreement. The maximum deflection values of the LFB and HFB are 12.6 and 0.38 mm, respectively. Both static responses showed a threshold separation distance d_{th} of 15 mm that divides the static profiles into the monostable region ($d > d_{th}$) and bistable region ($d < d_{th}$). For the monostable regime, a single stable equilibrium solution is shown. In contrast, in the bistable regime, each static response has two stable (upper and lower) branches and one unstable branch (middle). The effect of the weight of each tip mass is shown as a symmetry-breaking bifurcation phenomenon at the threshold distance.

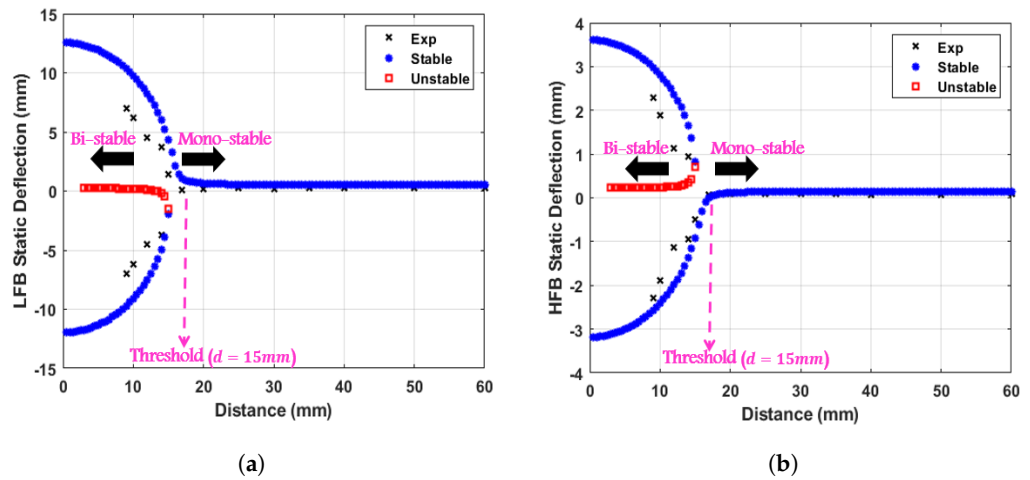


Figure 5. Experimental and theoretical static response of the (a) LFB, and (b) HFB. The threshold distance, d_{th} , was found to be 15 mm.

5.2. Dynamic Analysis

In this section, we will discuss how the magnetic force affects the natural frequency fluctuation of the nonlinear harvester. Toward this, the total deflections of the beams will be based on the static and dynamics deflections as follows:

$$\begin{aligned} z_1 &= z_{1s} + z_{1u} \\ z_2 &= z_{2s} + z_{2u} \end{aligned} \tag{8}$$

where z_{1u} and z_{2u} are the dynamic deflection of the LFB and HFB, respectively. The total vertical deflection is:

$$\begin{aligned} Y &= Y_s + Y_u \\ Y_u &= z_{1u} + z_{2u} \end{aligned} \tag{9}$$

Then, the magnetic force is:

$$F_{magy} = \frac{F_R(Y_s + Y_u)}{(d^2 + (Y_s + Y_u)^2)^{5/2}} \tag{10}$$

Using Taylor’s series around zero dynamic deflection ($Y_u = 0$), the magnetic force was expanded up to nine terms to avoid the complications of the magnetic formula in the numerical solution and guarantees the conversion of the numerical solution. This results in the following magnetic force:

$$\begin{aligned}
 F_{magy} &= F_{magys} + F_{magyu} \\
 F_{magy} &= \frac{F_R Y_s}{(d^2 + Y_s^2)^{5/2}} + \sum_{i=1}^9 \alpha_i Y_u^i(t), \quad i = 1, 2, \dots, 9
 \end{aligned}
 \tag{11}$$

where α_i are the coefficients of Taylor’s series expansion of the dynamic magnetic force [59]. Then, by taking the first linear term of the expanded F_{magy} and substituting it in Equation (3), the governing equation of the system will be:

$$\begin{cases}
 m_1 \ddot{z}_{1u}(t) + c_1 \dot{z}_{1u}(t) + (k_1 - \alpha_1) z_{1u}(t) - \alpha_1 z_{2u}(t) - F_{magyu} = m_1 a(t) \\
 m_2 \ddot{z}_{2u}(t) + c_2 \dot{z}_{2u}(t) + (k_2 + \alpha_1) z_{2u}(t) + \alpha_1 z_{1u}(t) + F_{magyu} + F_c = m_2 a(t) & z_2(t) < g_i \\
 m_2 \ddot{z}_{2u}(t) + c_2 \dot{z}_{2u}(t) + (k_2 + \alpha_1) z_{2u}(t) + \alpha_1 z_{1u}(t) + k_i (z_{2u}(t) - g_i) + F_{magyu} = m_2 a(t) & z_2(t) \geq g_i \\
 \dot{q} = -\frac{q(t)}{\epsilon_0 R S} \left(\frac{T}{\epsilon_r} + d_0 - z_{2u}(t) \right) + \frac{\sigma}{\epsilon_0 R S} (d_0 - z_{2u}(t))
 \end{cases}
 \tag{12}$$

Accordingly, the nonlinear natural frequencies of the LFB and HFB can be calculated from the following formulas:

$$f_1 = \frac{1}{2\pi} \sqrt{\frac{k_1 - \alpha_1}{m_1}} \quad f_2 = \frac{1}{2\pi} \sqrt{\frac{k_2 + \alpha_1}{m_2}}
 \tag{13}$$

where α_1 is the first linear term of the magnetic force after the expansion using Taylor’s series and is given by:

$$\alpha_1 = \frac{F_R (d^2 - 4Y_s^2)}{(d^2 + Y_s^2)^{7/2}}
 \tag{14}$$

5.2.1. Natural Frequencies

The variation of the nonlinear natural frequency with varying the magnets separation distance for both beams was extracted numerically using Equation (13) and experimentally by exciting the system at 0.05 g excitation level as shown in Figure 6. After that, the piece-wise curve fit functions were utilized to calculate the nonlinear natural frequencies variation with the magnets separation distance d for the LFB and HFB and then plotted as shown in Figure 7. The results show a threshold separation distance of 15 mm, consistent with findings from the static results in Figure 5. Moreover, the natural frequencies of both beams start to decrease to reach the minimum values at the threshold distance and then start to increase again with distances below the threshold distance. Moreover, the data in Figure 6 shows consistency between the simulation and experimental results in the monostable range, while it shows some discrepancies in the transition and bistable regimes. This discrepancy could be from different sources, such as the strong magnetic nonlinearity in the system, the lack of accuracy of the magnetic force equation used in the theoretical model, and the accuracy limitations of the lumped parameter modeling compared to the continuous modeling. Even though these discrepancies between the simulated and experimental results are minor, they would result in significant mismatch issues later when the dynamic behavior of the harvester is investigated. Therefore, to overcome these issues, the experimental results of the variation of the natural frequencies were used to extract the experimental stiffness values for both beams with curve fitting techniques to extract stiffness equations in piece-wise form as shown in Equations (15) and (16) for the LFB and HFB, respectively. The curve-fitting piece-wise equations are functions of the spacing distance between the two magnets. These stiffness equations were used to extract the variations of the natural frequencies for both the LFB and HFB and compared to the experimental results as shown in Figure 7. It is clearly shown that the previous discrepancies are removed, and it shows excellent matches for both LFB and HFB. Moreover, to enhance the accuracy of the analytical model while investigating the

system’s dynamic behavior, the stiffness terms $(k_1 - \alpha_1)$, and $(k_2 + \alpha_1)$ in Equation (12) will be replaced by (k_{LFB}) , and k_{HFB} , respectively.

$$k_{LFB} = \begin{cases} -21448 + 10055.9d - 1844.1d^2 + 167.2d^3 - 7.5d^4 + 0.1d^5 & \text{if } d < d_{th} \\ -336.1 + 43.2d - 1.6d^2 + 0.02d^3 + 4.0 \times 10^{-5}d^4 - 4.0 \times 10^{-6}d^5 + 2.5 \times 10^{-8}d^6 & \text{if } d \geq d_{th} \end{cases} \quad (15)$$

$$k_{HFB} = \begin{cases} -227.5 + 468.5d - 93.0d^2 + 8.0d^3 - 0.33d^4 + 0.01d^5 & \text{if } d < d_{th} \\ 112.3 + 26.8d - 1.1d^2 + 0.02d^3 - 2.0 \times 10^{-4}d^4 + 9.4 \times 10^{-7}d^5 & \text{if } d \geq d_{th} \end{cases} \quad (16)$$

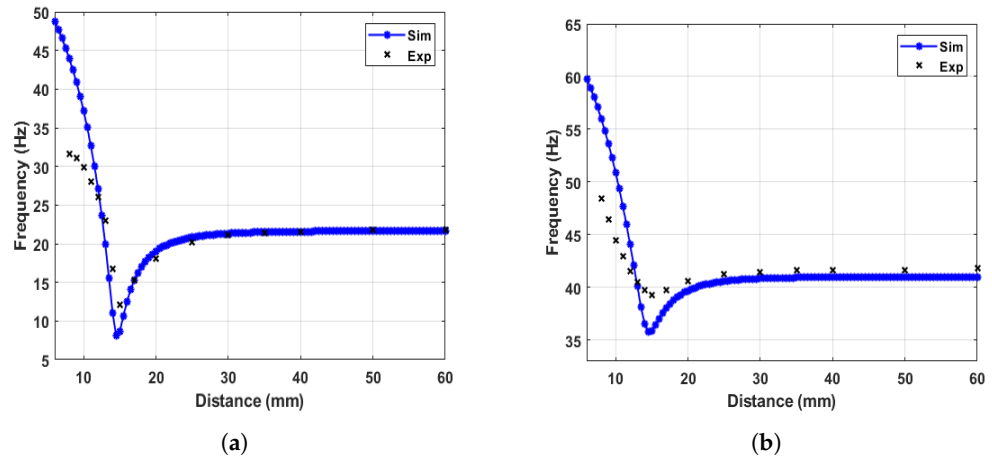


Figure 6. The simulated and experimental variations of the nonlinear natural frequency with magnet spacing for (a) LFB, (b) HFB.

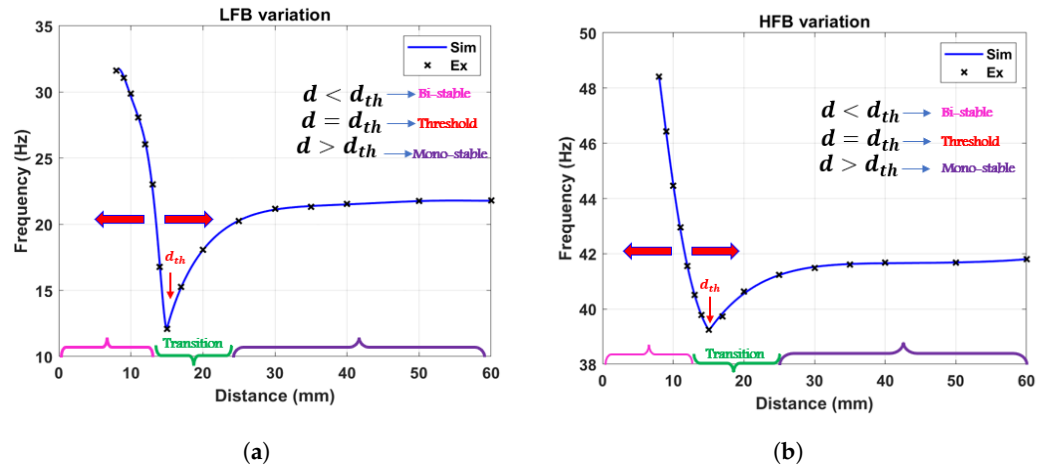


Figure 7. The simulated and experimental variations of the nonlinear natural frequency with magnet spacing using curve fit equations for (a) LFB, (b) HFB.

5.2.2. Linear Results

By removing the influence of the magnetic force ($F_{magy} = 0$), the linear response of the system and the generated voltage can be extracted. The experimental and simulated frequency response curves of the LFB and HFB at a low excitation level of 0.05 g are shown with good agreement in Figure 8. It can be noticed that the linear natural frequencies of the LFB and HFB are found to be (21.8 Hz) and (41 Hz), respectively. Moreover, the corresponding frequency voltage curve for the HFB is shown in Figure 8c, reflecting a maximum output voltage of 0.35 V. Furthermore, by focusing on the low-frequency range in Figure 8c, it is clear that there is no generated electrical signal at the LFB range due to eliminating the magnetic effect, and no interaction between the beams occurs.

The periodic motion in the structure generates electric charges to the surfaces of triboelectric materials. The generated electrical charges depend on the surface charge

density (σ), which is a function of the chemical properties of the materials and the micro-surface patterns that define the contact area [62]. Therefore, introducing micropatterns increases contact surfaces and enhances conversion efficiency [63]. Moreover, the amount of pressure applied on the triboelectric layers can play a role in the magnitude of the surface charge density. However, the surface charge density shows variations with time, so it is complicated to measure this value. Moreover, damping arises from removing energy by radiation or dissipation, and it is generally measured under cyclic or near-cyclic motion conditions. However, the damping factor varies as a function of frequency and excitations. Therefore, in our analysis and for simplifications, the surface charge density and damping values will be reported for each case separately.

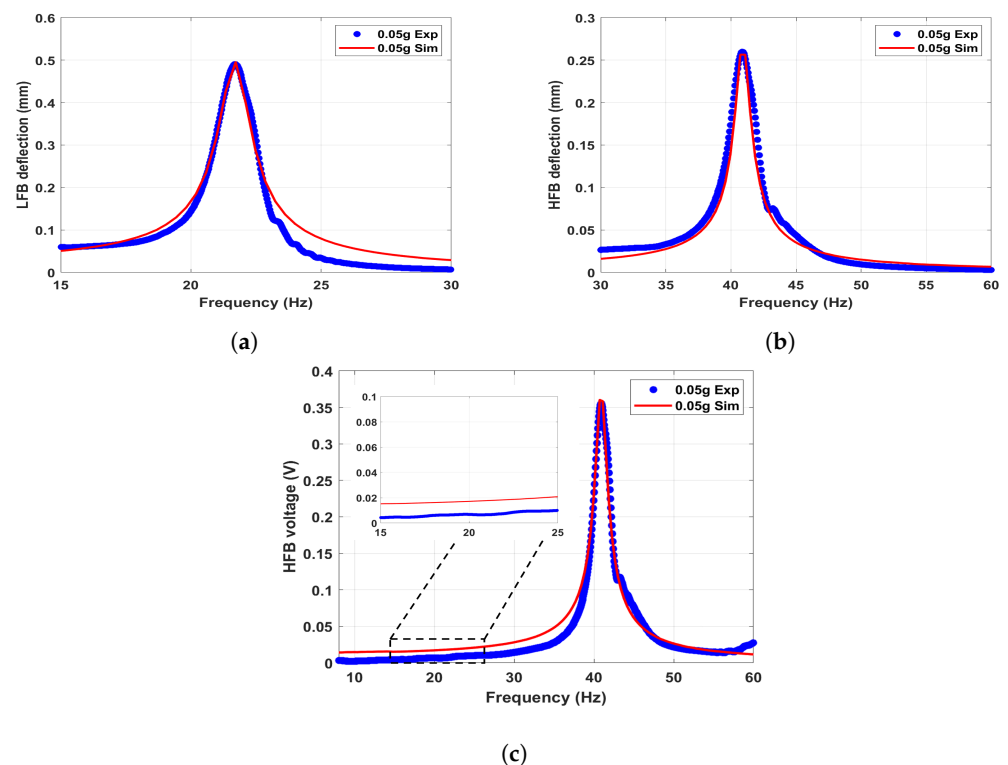


Figure 8. The linear simulated and experimental results at a low excitation level of 0.05 g: (a) frequency response curve of the LFB; (b) frequency response curve of the HFB; and (c) frequency voltage curve of the HFB. $c_1 = 0.04$, $c_2 = 0.039$, and $\sigma = 1 \mu\text{C}/\text{m}^2$.

5.2.3. Nonlinear Results

The energy harvester's dynamic behavior under the magnetic force's effect at the monostable, transition, and bistable regimes will be examined in this section. The triboelectric generator was attached to the HFB, while the generated electrical voltage signal was monitored at the LFB range to achieve the concept of frequency up-converter due to the magnetic coupling effect. The generated frequency–voltage curves were extracted at the three regimes under different excitation levels to demonstrate the frequency up-converter concept and investigate the effect of the magnetic force on the system's dynamic behavior.

The analysis will begin with the monostable regime and start with a large magnets separation distance of $d = 60$ mm. The corresponding experimental and theoretical results of the frequency–voltage and power curves under different excitation levels are shown in Figure 9. At the HFB range, the system acts linearly at a low excitation level. For example, it can be noticed that at a low excitation level of 0.1–0.3 g, the results are very close to the linear response results shown in Figure 8c. This is because the excitation level is very small, and the generated voltage is due to the capacitance effect between the triboelectric generator's electrodes. However, increasing the excitation level above 0.3 g, an impact between the harvester layers starts at the HFB range (around 40 Hz), resulting in higher

bandwidth and amplitudes. On the other hand, at the range of the LFB (around 22 Hz), even though the magnetic force is considered weak at this distance, the influence of the magnetic interaction is clearly shown by the new show-up voltage signal generated at this range as shown in Figure 9b. The newly generated voltage signal at the LFB range, even though the triboelectric generator was attached to the HFB, is proof of the concept of the frequency-up conversion. Furthermore, increasing the excitation level also leads to a noticed increment in the generated voltage and power signals, reaching a maximum value of 0.06 V at the 1.2 g excitation level. In contrast, a maximum value of 0.33 nW was achieved in the generated power at the same g level. However, the amplitude at $d = 60$ mm is minimal since the magnetic interaction is fragile at this large distance.

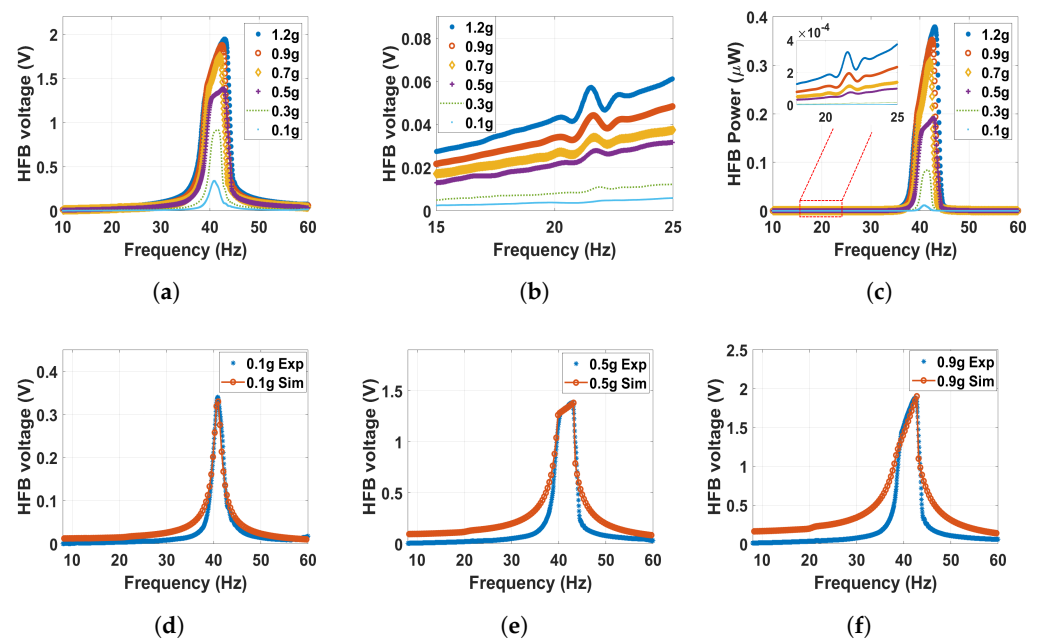


Figure 9. The frequency voltage curve of the HFB at different excitation levels with 60 mm separation distance: (a) experiment results in full range; (b) experiment results with zoom in at the LFB range; (c) experiment power results of the HFB; (d) experimental validation of the model at 0.1 g, $c_1 = 0.1$, $c_2 = 0.05$, and $\sigma = 3.5 \mu\text{C}/\text{m}^2$; (e) experimental validation of the model at 0.5 g, $c_1 = 0.1$, $c_2 = 0.045$, and $\sigma = 5.6 \mu\text{C}/\text{m}^2$; (f) experimental validation of the model at 0.9 g, $c_1 = 0.08$, $c_2 = 0.11$, and $\sigma = 5.15 \mu\text{C}/\text{m}^2$.

In order to study the dynamic behavior in the monostable regime, but at a more substantial magnetic force effect, the distance between the two magnets was set to 30 mm. The outcomes are shown in Figure 10, where the experimentally extracted frequency voltage curves are well-matched with simulations of the theoretical model. Moreover, it can be noticed that the natural frequencies of both beams are slightly shifted to the left in comparison with the linear natural frequencies to reach approximately 21 and 40.6 Hz for the LFB and HFB, respectively, indicating a softening behavior. This softening behavior is due to the effect of changing the separation distance (d) in the term α_1 according to Equations (13) and (14). Moreover, at higher excitation levels, the natural frequencies shifted more to the left to show significant softening behavior. This shift at higher excitation is due to the effect of the quadratic nonlinearity from the magnetic force. Moreover, the output voltage and power amplitudes increased with high excitation levels. The voltage at 1.2 g is maximized at 0.13 V at the LFB range, while the output power is maximized at 1.6 nW, which is higher than the values achieved at a 60 mm separation distance. After that, the separation distance is reduced to 25 mm. The corresponding matched experimental and theoretical frequency voltage and power curves are shown for different excitation levels in Figure 11. The results at this distance are close to the previous distance. However, we can notice here that the natural frequency is shifted more to the left, and the shifting increases

with higher excitation levels to indicate a softening behavior. In addition, the magnetic force is magnified as the separation distance decreases, resulting in higher interaction between the two beams leading to a higher output voltage and power, which peaked at approximately 0.28 and 7.9 nW at the LFB range, respectively, which are significantly higher than the previous values.

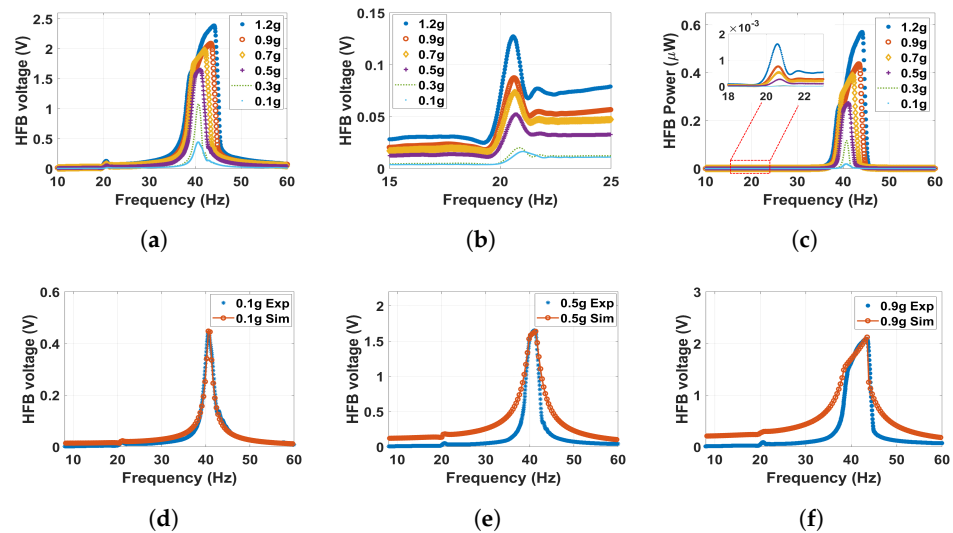


Figure 10. The frequency voltage curve of the HFB at different excitation levels with 30 mm separation distance: (a) experiment results in full range; (b) experiment results with zoom in at the LFB range; (c) experiment power results of the HFB; (d) experimental validation of the model at 0.1 g, $c_1 = 0.01$, $c_2 = 0.04$, and $\sigma = 3.9 \mu\text{C}/\text{m}^2$; (e) experimental validation of the model at 0.5 g, $c_1 = 0.02$, $c_2 = 0.09$, and $\sigma = 6.9 \mu\text{C}/\text{m}^2$; (f) experimental validation of the model at 0.9 g, $c_1 = 0.03$, $c_2 = 0.09$, and $\sigma = 6.7 \mu\text{C}/\text{m}^2$.

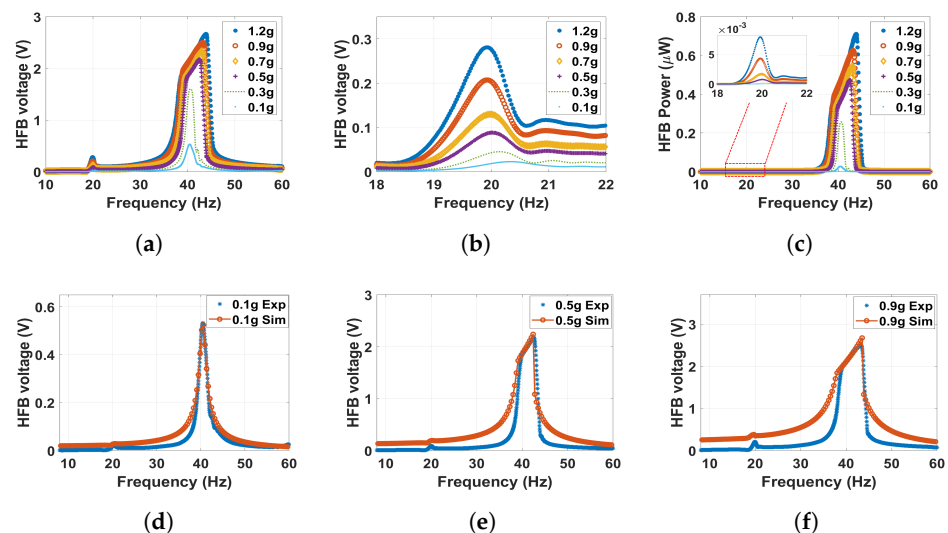


Figure 11. The frequency voltage curve of the HFB at different excitation levels with 25 mm separation distance: (a) experiment results in full range; (b) experiment results with zoom in at the LFB range; (c) experiment power results of the HFB; (d) experimental validation of the model at 0.1 g, $c_1 = 0.02$, $c_2 = 0.05$, and $\sigma = 5.5 \mu\text{C}/\text{m}^2$; (e) experimental validation of the model at 0.5 g, $c_1 = 0.03$, $c_2 = 0.03$, and $\sigma = 7.5 \mu\text{C}/\text{m}^2$; (f) experimental validation of the model at 0.9 g, $c_1 = 0.04$, $c_2 = 0.08$, and $\sigma = 8 \mu\text{C}/\text{m}^2$.

Next, the separation distance decreased to 20 mm, and the frequency–voltage curves from both the experiment and simulation are in good agreement as shown in Figure 12. At this distance, the system will enter the transition regime from the monostable side.

The results depicted in Figure 12 show that the natural frequency is shifted more to the left compared to the previous cases, reaching a lower value of 18.3 and 39.8 Hz for the LFB and HFB, respectively, which indicates a softening behavior. This shift results from the increased quadratic term of the magnetic nonlinearity at this distance in contrast to previous cases. In addition, it can be noticed in Figure 12b that the natural frequency of the LFB shifted more to the left with the increment in the excitation level, indicating a softening behavior, while increasing the excitation level to higher values will lead to a slight shift to the right indicating a hardening behavior. This exchange in the behavior is because at lower excitations, the quadratic nonlinearity is more dominant in the system, and a softening behavior is shown. On the other hand, when the excitation level increases, the cubic magnetic nonlinearity becomes more dominant, and a hardening behavior is shown. Moreover, as the excitation level increases, the output voltage rises due to the combined effect of the higher impact between the harvester layers at these higher excitation levels and the influence of the magnetic force. Furthermore, when compared to the monostable regime with a maximum output voltage of 0.48 V at the 1.2 g level of excitation, the output voltage at this distance increased by 700% in the LFB range. The last thing that can be noticed is that the power of the LFB at this distance peaked at 0.02 W at the 1.2 g excitation level as shown in Figure 12c, which is significantly higher than the values of the previous distances.

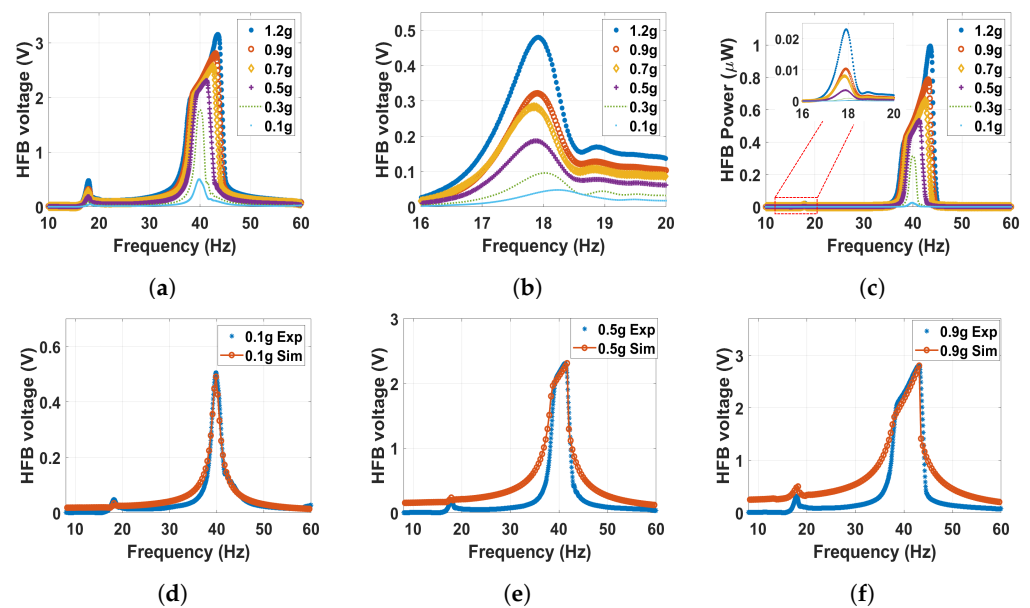


Figure 12. The frequency voltage curve of the HFB at different excitation levels with 20 mm separation distance: (a) experiment results in full range; (b) experiment results with zoom in at the LFB range; (c) experiment power results of the HFB; (d) experimental validation of the model at 0.1 g, $c_1 = 0.02$, $c_2 = 0.05$, and $\sigma = 5 \mu\text{C}/\text{m}^2$; (e) experimental validation of the model at 0.5 g, $c_1 = 0.03$, $c_2 = 0.05$, and $\sigma = 8.5 \mu\text{C}/\text{m}^2$; (f) experimental validation of the model at 0.9 g, $c_1 = 0.055$, $c_2 = 0.09$, and $\sigma = 7.9 \mu\text{C}/\text{m}^2$.

Now, the separation distance is reduced to 17 mm, which is still in the transition regime but from the monostable side. The experiment and simulation's frequency voltage and power curves are shown in Figure 13 with a good agreement. The natural frequencies are shifted to the left, indicating a nonlinear softening behavior because of the dominance of quadratic nonlinearity. This significant shift is because the magnetic force between the two beams' tip magnets becomes stronger in this case. Moreover, increasing the excitation level shifts the natural frequency to the right to achieve hardening behavior because of the dominance of cubic nonlinearity. In addition, higher output voltage with an increment of 867% can be achieved in the LFB range compared with the monostable regime to reach a maximum value of 0.58 V at the 1.2 g excitation level. Finally, it can be noticed from

Figure 13c that the generated power maximized at 0.033 W at the 1.2 g level of excitation.

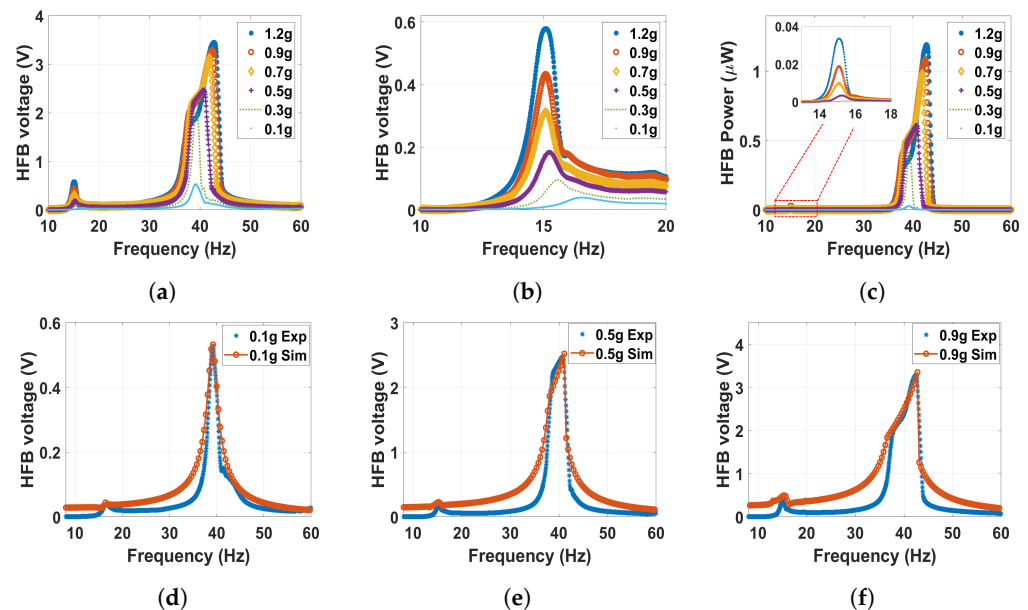


Figure 13. The frequency voltage curve of the HFB at different excitation levels with 17 mm separation distance: (a) experiment results in full range; (b) experiment results with zoom in at the LFB range; (c) experiment power results of the HFB; (d) experimental validation of the model at 0.1 g, $c_1 = 0.02$, $c_2 = 0.07$, and $\sigma = 7.5 \mu\text{C}/\text{m}^2$; (e) experimental validation of the model at 0.5 g, $c_1 = 0.06$, $c_2 = 0.05$, and $\sigma = 8 \mu\text{C}/\text{m}^2$; (f) experimental validation of the model at 0.9 g, $c_1 = 0.07$, $c_2 = 0.05$, and $\sigma = 8 \mu\text{C}/\text{m}^2$.

By lowering the separation distance to reach the threshold at $d_{th} = 15$ mm, the experimental and simulated frequency–voltage and power curves are shown in Figure 14. The maximum possible shift to the left in natural frequencies is achieved to reach the lowest value of 38.5 and 11.7 Hz for the HFB and LFB, respectively, which indicates a significant softening behavior. However, increasing the excitation level shifts the frequency to the right, indicating a hardening behavior. The maximum corresponding output voltage at the LFB range is 0.73 V at the 1.2 g level of excitation, where there is no increase in the output voltage signal compared with the previous distance at the same g level. Moreover, Figure 14c shows that the maximum power in the LFB range is 0.05 W at the 1.2 g level of excitation. The threshold distance achieved a maximum generated output voltage and power compared to all previous cases. Further decrease in the distance to 14.5 mm is still in the transition regime but from the bistable side. The frequency–voltage curves extracted experimentally agree with the ones extracted theoretically, as shown in Figure 15. The natural frequency for both beams shifted to the left in comparison with the linear natural frequency of each beam to reach 38.9 and 12 Hz for the HFB and LFB, respectively, indicating a softening behavior. Moreover, it can be noticed that the generated voltage dropped at this distance if it is compared with the threshold distance results in Figure 14. This is because the magnetic nonlinearity becomes very strong, producing less impact between the triboelectric layers, which means less output voltage. Therefore, higher excitation levels are needed to increase the impact between the triboelectric layers and generate electricity. However, the maximum voltage peaked at 0.33 V at the LFB range with the 1.2 g excitation level. However, the maximum power in the LFB range achieved at this distance is 0.01 W at the 1.2 g level of excitation as shown in Figure 15c.

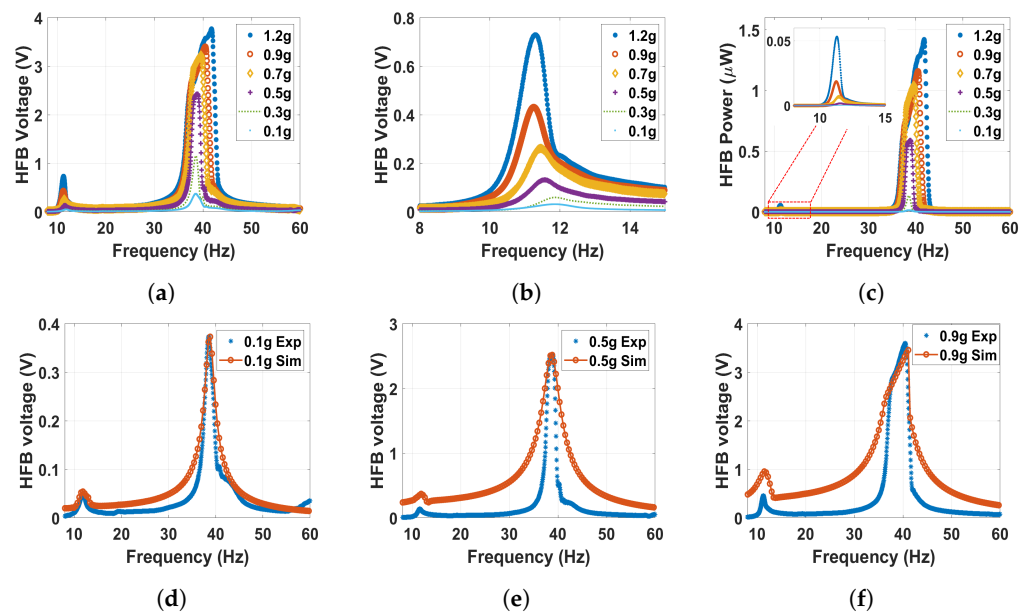


Figure 14. The frequency voltage curve of the HFB at different excitation levels with 15 mm separation distance: (a) experiment results in full range; (b) experiment results with zoom in at the LFB range; (c) experiment power results of the HFB; (d) experimental validation of the model at 0.1 g, $c_1 = 0.07$, $c_2 = 0.07$, and $\sigma = 5.2 \mu\text{C}/\text{m}^2$; (e) experimental validation of the model at 0.5 g, $c_1 = 0.1$, $c_2 = 0.12$, and $\sigma = 12 \mu\text{C}/\text{m}^2$; (f) experimental validation of the model at 0.9 g, $c_1 = 0.1$, $c_2 = 0.12$, and $\sigma = 10.7 \mu\text{C}/\text{m}^2$.

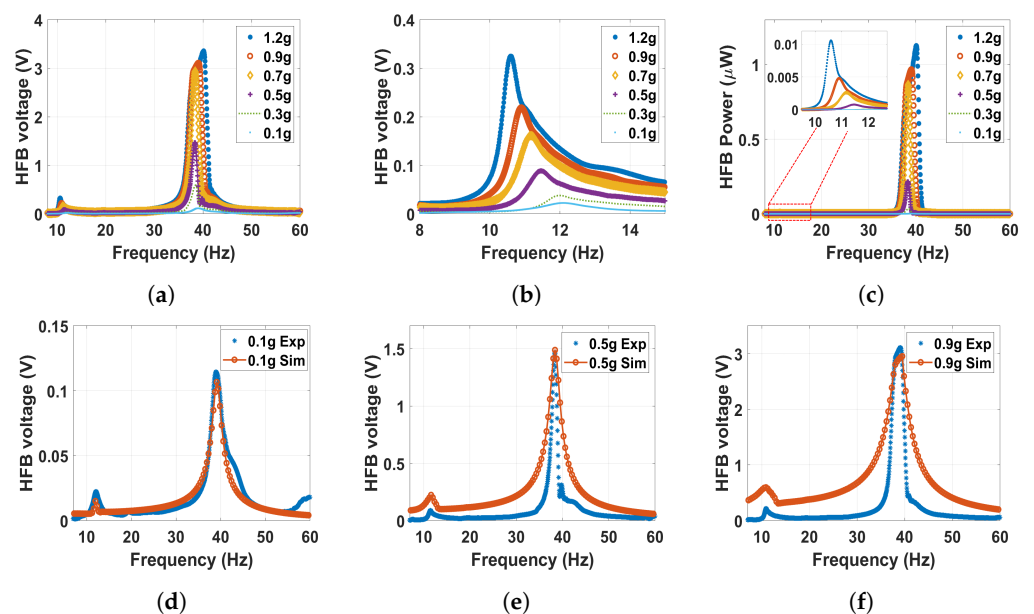


Figure 15. The frequency voltage curve of the HFB at different excitation levels with 14.5 mm separation distance: (a) experiment results in full range; (b) experiment results with zoom in at the LFB range; (c) experiment power results of the HFB; (d) experimental validation of the model at 0.1 g, $c_1 = 0.03$, $c_2 = 0.07$, and $\sigma = 1.5 \mu\text{C}/\text{m}^2$; (e) experimental validation of the model at 0.5 g, $c_1 = 0.08$, $c_2 = 0.075$, and $\sigma = 4.4 \mu\text{C}/\text{m}^2$; (f) experimental validation of the model at 0.9 g, $c_1 = 0.12$, $c_2 = 0.12$, and $\sigma = 8.2 \mu\text{C}/\text{m}^2$.

Experimentally, at lower separation distances below 14.5 mm, the magnetic force becomes very strong and causes the beam to stick to the fixed electrode, which could lead to failure in the system and no electrical signal generated. Therefore, the dynamic behavior of the harvester for lower distances is extracted theoretically since we already validated

our theoretical model in all the previous cases. In light of this, the distance decreased to reach 12 mm, and the results of the frequency voltage and power curves of the HFB with the zoomed response in the LFB range are shown in Figure 16. The results show that the natural frequencies are shifted to the right to higher values of 26.3 and 41.5 Hz for the LFB and HFB, respectively, indicating a hardening behavior. Moreover, it can be noticed that the output voltage and power dropped significantly to 0.23 V and 5.4 nW, respectively, in the LFB range in comparison with the previous case. This drop could be due to the system's high nonlinearity, which makes the beam behave stiffer, and less impact between the triboelectric layers occurs, hence generating less voltage. Moreover, we can notice the appearance of the subharmonic resonance shown at ($\omega_{n1}/2 = 13.74$ Hz, $\omega_{n2}/2 = 20.58$ Hz) due to high nonlinearity and the dominance of the quadratic nonlinearity in the system.

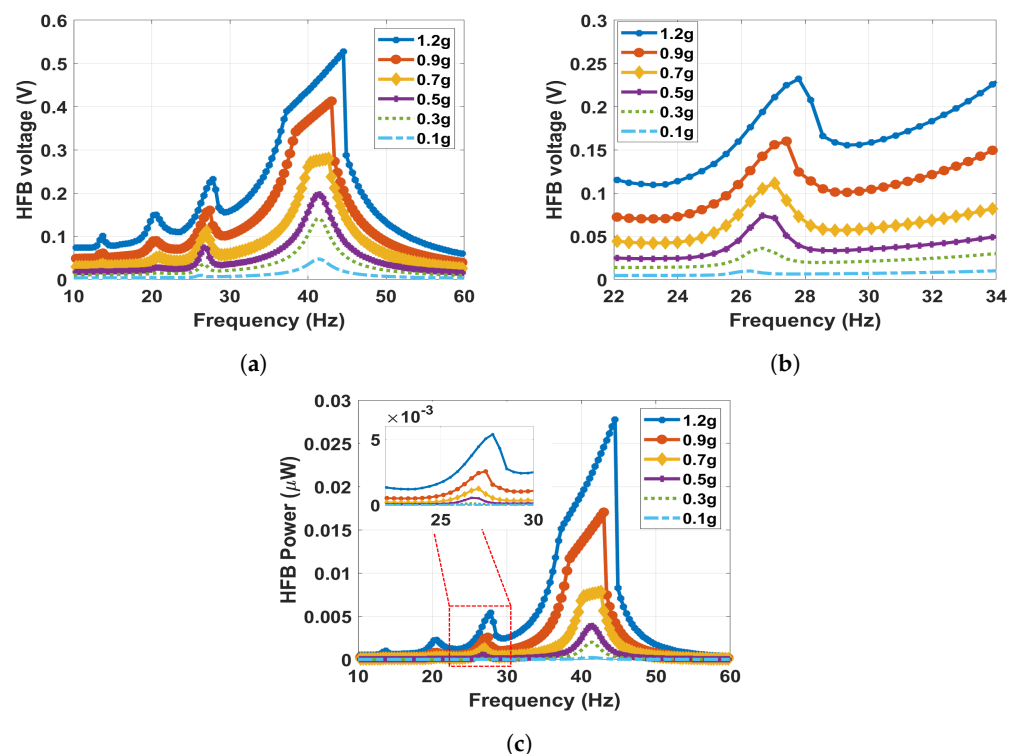


Figure 16. The frequency voltage curve of the HFB at different excitation levels with 12 mm separation distance: (a) simulated results in full range; (b) simulated results with zoom in at the LFB range, $\sigma = 1.7 \mu\text{C}/\text{m}^2$; (c) simulated power results of the HFB.

To summarize the results discussed above and to specify the optimal operating regime, the output voltage and power at the LFB range were calculated and plotted versus the magnets' separation distance at different excitation levels, as shown in Figure 17. The output voltage and power are maximized at the transition regime, particularly at the threshold distance at high excitation levels. Even though, at low excitation levels, the transition regime is still the most suitable for harvesting energy.

We utilized vibro-impact triboelectric transducers with magnetic nonlinearity to create a nonlinear frequency up-converter under harmonic excitations. This study focuses on combining magnetic nonlinearity with the inherent phenomenon of vibro-impact in triboelectric energy harvesters to transfer the energy between low and high oscillations. The combination of magnetic nonlinearity and vibro-impact is a novel strategy for triboelectric energy harvesters' applications. Moreover, the addition of magnetic nonlinearity makes the harvester variable frequency energy harvester, where the operating frequency can be controlled by controlling the distance between the two magnets to target multiple applications at different frequency ranges.

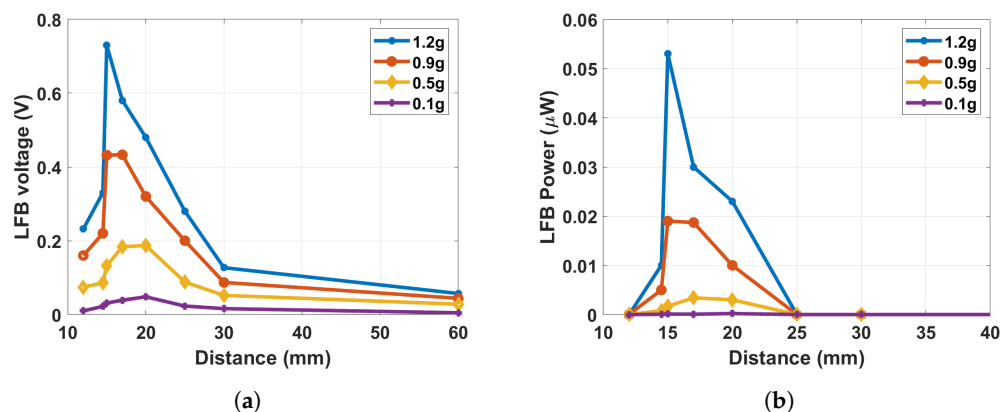


Figure 17. (a) The output voltage in the LFB range versus the separation distance at different excitation levels; (b) The output power in the LFB range versus the separation distance at different excitation levels.

6. Conclusions

In summary, a frequency up-converter using a vibro-impact triboelectric energy harvester efficiently converts low-frequency vibrations to a higher frequency is demonstrated. The system comprises low-frequency and high-frequency beams with two identical attached tip magnets. The magnetic coupling transfers the energy between the high-frequency and low-frequency ranges and generates a voltage signal at the LFB even though the generator was attached to the HFB, indicating a frequency up-converter. The structure was tested experimentally and validated with the simulated results of the theoretical model with good agreement. Different nonlinear behaviors of softening and hardening have been achieved by controlling the distance between the two magnets. Furthermore, a significant increment in the output voltage signal was achieved by lowering the distance between the two magnets. Moreover, the transition region was the optimum region to obtain the maximum voltage. Triboelectricity shows high efficiency in frequency up-conversion applications.

Author Contributions: Methodology, H.A. and A.I.; Software, H.A.; Validation, H.A.; Investigation, A.I.; Data curation, H.A. and A.I.; Writing—original draft, H.A.; Writing—review & editing, H.A. and A.I.; Visualization, A.I.; Supervision, A.I.; Project administration, A.I. All authors have read and agreed to the published version of the manuscript.

Funding: This research received no external funding.

Data Availability Statement: Data available on request from the authors.

Conflicts of Interest: The authors declare no conflict of interest.

References

- Sullivan, J.; Gaines, L. *A Review of Battery Life-Cycle Analysis: State of Knowledge and Critical Needs*; Argonne National Lab. (ANL): Argonne, IL, USA, 2010.
- Abdin, Z.; Alim, M.; Saidur, R.; Islam, M.; Rashmi, W.; Mekhilef, S.; Wadi, A. Solar energy harvesting with the application of nanotechnology. *Renew. Sustain. Energy Rev.* **2013**, *26*, 837–852. [[CrossRef](#)]
- Ibrahim, H.; Singh, M.; Al-Bawri, S.; Ibrahim, S.; Islam, M.; Alzamil, A.; Islam, M. Radio frequency energy harvesting technologies: A comprehensive review on designing, methodologies, and potential applications. *Sensors* **2022**, *22*, 4144. [[CrossRef](#)] [[PubMed](#)]
- Cuadras, A.; Gasulla, M.; Ferrari, V. Thermal energy harvesting through pyroelectricity. *Sens. Actuators Phys.* **2010**, *158*, 132–139. [[CrossRef](#)]
- Ambrożkiewicz, B.; Litak, G.; Wolszczak, P. Modelling of electromagnetic energy harvester with rotational pendulum using mechanical vibrations to scavenge electrical energy. *Appl. Sci.* **2020**, *10*, 671. [[CrossRef](#)]
- Hassan, M.; Baker, K.; Ibrahim, A. Modeling of triboelectric vibration energy harvester under rotational magnetic excitation. *Smart Mater. Adapt. Struct. Intell. Syst.* **2021**, *85499*, V001T04A012.
- Zhang, L.; Zhang, B.; Chen, J.; Jin, L.; Deng, W.; Tang, J.; Zhang, H.; Pan, H.; Zhu, M.; Yang, W.; et al. Lawn structured triboelectric nanogenerators for scavenging sweeping wind energy on rooftops. *Adv. Mater.* **2016**, *28*, 1650–1656. [[CrossRef](#)]

8. Chen, X.; Gao, L.; Chen, J.; Lu, S.; Zhou, H.; Wang, T.; Wang, A.; Zhang, Z.; Guo, S.; Mu, X.; et al. A chaotic pendulum triboelectric-electromagnetic hybridized nanogenerator for wave energy scavenging and self-powered wireless sensing system. *Nano Energy* **2020**, *69*, 104440. [[CrossRef](#)]
9. Roundy, S.; Wright, P.; Rabaey, J. A study of low level vibrations as a power source for wireless sensor nodes. *Comput. Commun.* **2003**, *26*, 1131–1144. [[CrossRef](#)]
10. Miller, L.; Halvorsen, E.; Dong, T.; Wright, P. Modeling and experimental verification of low-frequency MEMS energy harvesting from ambient vibrations. *J. Micromech. Microeng.* **2011**, *21*, 045029. [[CrossRef](#)]
11. Vidal, J.; Slabov, V.; Kholkin, A.; Dos Santos, M. Hybrid triboelectric-electromagnetic nanogenerators for mechanical energy harvesting: A review. *Nano Micro Lett.* **2021**, *13*, 199. [[CrossRef](#)]
12. Dong, L.; Closson, A.; Jin, C.; Trase, I.; Chen, Z.; Zhang, J. Vibration-Energy-Harvesting System: Transduction Mechanisms, Frequency Tuning Techniques, and Biomechanical Applications. *Adv. Mater. Technol.* **2019**, *4*, 1900177. [[CrossRef](#)] [[PubMed](#)]
13. Hassena, M.; Samaali, H.; Ouakad, H.; Najjar, F. Arched Beam Based Energy Harvester Using Electrostatic Transduction for General in-plane Excitations. In Proceedings of the 2021 18th International Multi-Conference on Systems, Signals & Devices (SSD), Monastir, Tunisia, 22–25 March 2021; pp. 210–215.
14. Atmeh, M.; Ibrahim, A. Modeling of Piezoelectric Vibration Energy Harvesting From Low-Frequency Using Frequency Up-Conversion. *Smart Mater. Adapt. Struct. Intell. Syst.* **2021**, *85499*, V001T04A011.
15. Miao, G.; Fang, S.; Wang, S.; Zhou, S. A low-frequency rotational electromagnetic energy harvester using a magnetic plucking mechanism. *Appl. Energy* **2022**, *305*, 117838. [[CrossRef](#)]
16. Foong, F.; Thein, C.; Yurchenko, D. Structural optimisation through material selections for multi-cantilevered vibration electromagnetic energy harvesters. *Mech. Syst. Signal Process.* **2002**, *162*, 08044. [[CrossRef](#)]
17. Ibrahim, A.; Ramini, A.; Towfighian, S. Experimental and theoretical investigation of an impact vibration harvester with triboelectric transduction. *J. Sound Vib.* **2018**, *416*, 111–124. [[CrossRef](#)]
18. Zargari, S.; Koozehkanani, Z.; Veladi, H.; Sobhi, J.; Rezaia, A. A new Mylar-based triboelectric energy harvester with an innovative design for mechanical energy harvesting applications. *Energy Convers. Manag.* **2021**, *244*, 114489. [[CrossRef](#)]
19. Ibrahim, A.; Hassan, M. Extended bandwidth of 2DOF double impact triboelectric energy harvesting: Theoretical and experimental verification. *Appl. Energy* **2023**, *333*, 120593. [[CrossRef](#)]
20. Fan, F.; Tian, Z.; Wang, Z. Flexible triboelectric generator. *Nano Energy* **2012**, *1*, 328–334. [[CrossRef](#)]
21. Bertacchini, A.; Larcher, L.; Lasagni, M.; Pavan, P. Ultra Low Cost Triboelectric Energy Harvesting Solutions for Embedded Sensor Systems. In Proceedings of the 2015 IEEE 15th International Conference on Nanotechnology (IEEE-NANO), Rome, Italy, 27–30 July 2015; pp. 1151–1154.
22. He, W.; Fu, X.; Zhang, D.; Zhang, Q.; Zhuo, K.; Yuan, Z.; Ma, R. Recent progress of flexible/wearable self-charging power units based on triboelectric nanogenerators. *Nano Energy* **2021**, *84*, 105880. [[CrossRef](#)]
23. Rahman, M.; Rana, S.; Salauddin, M.; Maharjan, P.; Bhatta, T.; Park, J. Biomechanical energy-driven hybridized generator as a universal portable power source for smart/wearable electronics. *Adv. Energy Mater.* **2020**, *10*, 1903663. [[CrossRef](#)]
24. Zhang, C.; Zhang, L.; Bao, B.; Ouyang, W.; Chen, W.; Li, Q.; Li, D. Customizing Triboelectric Nanogenerator on Everyday Clothes by Screen-Printing Technology for Biomechanical Energy Harvesting and Human-Interactive Applications. *Adv. Mater. Technol.* **2023**, *8*, 2201138. [[CrossRef](#)]
25. Zhao, H.; Ouyang, H. Theoretical investigation and experiment of a disc-shaped triboelectric energy harvester with a magnetic bistable mechanism. *Smart Mater. Struct.* **2021**, *30*, 095026. [[CrossRef](#)]
26. Rana, S.; Rahman, M.; Salauddin, M.; Sharma, S.; Maharjan, P.; Bhatta, T.; Cho, H.; Park, C.; Park, J. Electrospun PVDF-TrFE/MXene nanofiber mat-based triboelectric nanogenerator for smart home appliances. *ACS Appl. Mater. Interfaces* **2021**, *13*, 4955–4967. [[CrossRef](#)] [[PubMed](#)]
27. Li, W.; Sengupta, D.; Pei, Y.; Kottapalli, A. Wearable Nanofiber-Based Triboelectric Nanogenerator for Body Motion Energy Harvesting. In Proceedings of the 2021 IEEE International Conference on Flexible and Printable Sensors and Systems (FLEPS), Manchester, UK, 20–23 June 2021; pp. 1–4.
28. Zu, G.; Wei, Y.; Sun, C.; Yang, X. Humidity-resistant, durable, wearable single-electrode triboelectric nanogenerator for mechanical energy harvesting. *J. Mater. Sci.* **2022**, *57*, 2813–2824. [[CrossRef](#)]
29. Han, X.; Jiang, D.; Qu, X.; Bai, Y.; Cao, Y.; Luo, R.; Li, Z. A stretchable, self-healable triboelectric nanogenerator as electronic skin for energy harvesting and tactile sensing. *Materials* **2021**, *14*, 1689. [[CrossRef](#)] [[PubMed](#)]
30. Yu, J.; Hou, X.; He, J.; Cui, M.; Wang, C.; Geng, W.; Mu, J.; Han, B.; Chou, X. Ultra-flexible and high-sensitive triboelectric nanogenerator as electronic skin for self-powered human physiological signal monitoring. *Nano Energy* **2020**, *69*, 104437. [[CrossRef](#)]
31. Hossain, N.; Yamomo, G.; Willing, R.; Towfighian, S. Characterization of a packaged triboelectric harvester under simulated gait loading for total knee replacement. *IEEE/ASME Trans. Mechatron.* **2021**, *26*, 2967–2976. [[CrossRef](#)]
32. Atmeh, M.; Athey, C.; Ramini, A.; Barakat, N.; Ibrahim, A. Performance analysis of triboelectric energy harvester designs for knee implants. *Health Monit. Struct. Biol. Syst.* **2021**, *11593*, 221–231.
33. Davis, J.; Atmeh, M.; Barakat, N.; Ibrahim, A. Design and performance simulation of a triboelectric energy harvester for total hip replacement implants. *Health Monit. Struct. Biol. Syst.* **2021**, *11593*, 232–244.

34. Real, F.; Batou, A.; Ritto, T.; Desceliers, C. Stochastic modeling for hysteretic bit–rock interaction of a drill string under torsional vibrations. *J. Vib. Control.* **2019**, *25*, 1663–1672. [[CrossRef](#)]
35. Chen, M.; Wang, Z.; Zheng, Y.; Zhang, Q.; He, B.; Yang, J.; Qi, M.; Wei, L. Flexible tactile sensor based on patterned Ag-nanofiber electrodes through electrospinning. *Sensors* **2021**, *21*, 2413. [[CrossRef](#)] [[PubMed](#)]
36. Min, G.; Dahiya, A.; Mulvihill, D.; Dahiya, R. A Wide Range Self-Powered Flexible Pressure Sensor Based on Triboelectric Nanogenerator. In Proceedings of the 2021 IEEE International Conference on Flexible and Printable Sensors and Systems (FLEPS), Manchester, UK, 20–23 June 2021; pp. 1–4.
37. Du, T.; Zuo, X.; Dong, F.; Li, S.; Mtui, A.; Zou, Y.; Zhang, P.; Zhao, J.; Zhang, Y.; Sun, P.; et al. A self-powered and highly accurate vibration sensor based on bouncing-ball triboelectric nanogenerator for intelligent ship machinery monitoring. *Micromachines* **2021**, *12*, 218. [[CrossRef](#)] [[PubMed](#)]
38. Wang, S.; Lin, L.; Xie, Y.; Jing, Q.; Niu, S.; Wang, Z. Sliding-triboelectric nanogenerators based on in-plane charge-separation mechanism. *Nano Lett.* **2013**, *13*, 2226–2233. [[CrossRef](#)]
39. Niu, S.; Liu, Y.; Wang, S.; Lin, L.; Zhou, Y.; Hu, Y.; Wang, Z. Theory of sliding-mode triboelectric nanogenerators. *Adv. Mater.* **2013**, *25*, 6184–6193. [[CrossRef](#)] [[PubMed](#)]
40. Yang, Y.; Zhang, H.; Chen, J.; Jing, Q.; Zhou, Y.; Wen, X.; Wang, Z. Single-electrode-based sliding triboelectric nanogenerator for self-powered displacement vector sensor system. *ACS Nano* **2013**, *7*, 7342–7351. [[CrossRef](#)]
41. Meng, B.; Tang, W.; Too, Z.; Zhang, X.; Han, M.; Liu, W.; Zhang, H. A transparent single-friction-surface triboelectric generator and self-powered touch sensor. *Energy Environ. Sci.* **2013**, *6*, 3235–3240. [[CrossRef](#)]
42. Niu, S.; Liu, Y.; Chen, X.; Wang, S.; Zhou, Y.; Lin, L.; Xie, Y.; Wang, Z. Theory of freestanding triboelectric-layer-based nanogenerators. *Nano Energy* **2015**, *12*, 760–774. [[CrossRef](#)]
43. Jiang, T.; Chen, X.; Han, C.; Tang, W.; Wang, Z. Theoretical study of rotary freestanding triboelectric nanogenerators. *Adv. Funct. Mater.* **2015**, *25*, 2928–2938. [[CrossRef](#)]
44. Yang, B.; Zeng, W.; Peng, Z.; Liu, S.; Chen, K.; Tao, X. A fully verified theoretical analysis of contact-mode triboelectric nanogenerators as a wearable power source. *Adv. Energy Mater.* **2016**, *6*, 1600505. [[CrossRef](#)]
45. Zhao, C.; Yang, Y.; Upadrashta, D.; Zhao, L. Design, modeling and experimental validation of a low-frequency cantilever triboelectric energy harvester. *Energy* **2021**, *214*, 118885. [[CrossRef](#)]
46. Erturk, A.; Inman, D. Broadband piezoelectric power generation on high-energy orbits of the bistable Duffing oscillator with electromechanical coupling. *J. Sound Vib.* **2011**, *330*, 2339–2353. [[CrossRef](#)]
47. Sari, I.; Balkan, T.; Kulah, H. A Wideband Electromagnetic Micro Power Generator for Wireless Microsystems. In Proceedings of the TRANSDUCERS 2007–2007 International Solid-State Sensors, Actuators and Microsystems Conference. Lyon, France, 10–14 June 2017; pp. 275–278.
48. Zou, H.; Zhao, L.; Gao, Q.; Zuo, L.; Liu, F.; Tan, T.; Wei, K.; Zhang, W. Mechanical modulations for enhancing energy harvesting: Principles, methods and applications. *Appl. Energy* **2019**, *255*, 113871. [[CrossRef](#)]
49. Brennan, M.; Gatti, G. Harvesting energy from time-limited harmonic vibrations: Mechanical considerations. *J. Vib. Acoust.* **2017**, *139*, 051019. [[CrossRef](#)]
50. Yang, G.; Stark, B.; Hollis, S.; Burrow, S. Challenges for energy harvesting systems under intermittent excitation. *IEEE J. Emerg. Sel. Top. Circuits Syst.* **2014**, *4*, 364–374. [[CrossRef](#)]
51. Li, X.; Hu, G.; Guo, Z.; Wang, J.; Yang, Y.; Liang, J. Frequency up-conversion for vibration energy harvesting: A review. *Symmetry* **2022**, *14*, 631. [[CrossRef](#)]
52. Fakeih, E. Harvesting Mechanical Vibrations Using a Frequency Up-Converter. Ph.D. Thesis, King Abdullah University of Science and Technology, Thuwal, Saudi Arabia, 2020.
53. Fakeih, E.; Almansouri, A.; Kosel, J.; Younis, M.; Salama, K. A Wideband Magnetic Frequency Up-Converter Energy Harvester. *Adv. Eng. Mater.* **2021**, 2001364. [[CrossRef](#)]
54. Gu, L.; Livermore, C. Impact-driven, frequency up-converting coupled vibration energy harvesting device for low frequency operation. *Smart Mater. Struct.* **2011**, *20*, 045004. [[CrossRef](#)]
55. Pozzi, M.; Zhu, M. Plucked piezoelectric bimorphs for energy harvesting. *Adv. Energy Harvest. Methods* **2013**, *2013*, 119–140.
56. Jung, S.; Yun, K. Energy-harvesting device with mechanical frequency-up conversion mechanism for increased power efficiency and wideband operation. *Appl. Phys. Lett.* **2010**, *96*, 111906. [[CrossRef](#)]
57. Cottone, F.; Gammaitoni, L.; Vocca, H.; Ferrari, M.; Ferrari, V. Piezoelectric buckled beams for random vibration energy harvesting. *Smart Mater. Struct.* **2012**, *21*, 035021. [[CrossRef](#)]
58. Yin, Z.; Gao, S.; Jin, L.; Guo, S.; Wu, Q.; Li, Z. A shoe-mounted frequency up-converted piezoelectric energy harvester. *Sens. Actuators Phys.* **2021**, *318*, 112530. [[CrossRef](#)]
59. Atmeh, M.; Ibrahim, A.; Ramini, A. Static and Dynamic Analysis of a Bistable Frequency Up-Converter Piezoelectric Energy Harvester. *Micromachines* **2023**, *14*, 261. [[CrossRef](#)] [[PubMed](#)]
60. Wang, Z. Triboelectric nanogenerators as new energy technology for self-powered systems and as active mechanical and chemical sensors. *ACS Nano* **2013**, *7*, 9533–9557. [[CrossRef](#)] [[PubMed](#)]
61. Younis, M. *MEMS Linear and Nonlinear Statics and Dynamics*; Springer Science & Business Media: Berlin, Germany, 2011.

62. Henniker, J. Triboelectricity in polymers. *Nature* **1962**, *196*, 474.
63. Dhakar, L.; Tay, F.; Lee, C. Development of a broadband triboelectric energy harvester with SU-8 micropillars. *J. Microelectromechanical Syst.* **2014**, *24*, 91–99. [[CrossRef](#)]

Disclaimer/Publisher's Note: The statements, opinions and data contained in all publications are solely those of the individual author(s) and contributor(s) and not of MDPI and/or the editor(s). MDPI and/or the editor(s) disclaim responsibility for any injury to people or property resulting from any ideas, methods, instructions or products referred to in the content.